University of Bath

Alternative formats

If you require this document in an alternative format, please contact:
openaccess@bath.ac.uk

VORTEX TRACKING OF PURGE-MAINSTREAM INTERACTIONS IN A ROTATING TURBINE STAGE

Alex W. Mesny[1]   Mark A. Glozier[1]   Oliver J. Pountney[1]   James A. Scobie[1]

Yan Sheng Li[2]   David J. Cleaver[1]   Carl M. Sangan[1]

[1]Department of Mechanical Engineering, University of Bath, Bath, United Kingdom.

[2]Siemens Industrial Turbomachinery Ltd., Lincoln, United Kingdom.

Corresponding Author's Email: c.m.sangan@bath.ac.uk

ABSTRACT

The use of purge flow in gas turbines allows for high turbine entry temperatures, which are essential to produce high cycle efficiency. Purge air is bled from the compressor and reintroduced in the turbine to cool vulnerable components. Wheel-spaces are formed between adjacent rotating and stationary discs, with purge air supplied at low radius before exiting into the mainstream gas-path through a rim-seal at the disc periphery. An aerodynamic penalty is incurred as the purge flow egress interacts with the mainstream. This study presents unparalleled three-dimensional velocity data from a single-stage turbine test rig, specifically designed to investigate egress-mainstream interaction using optical measurement techniques.

Volumetric Velocimetry is applied to the rotating environment with phase-locked measurements used to identify and track the vortical secondary flow features through the blade passage. A baseline case without purge flow is compared to experiments with a 1.7% purge mass fraction; the latter was chosen to ensure a fully sealed wheel-space. A non-localised vortex tracking function is applied to the data to identify the position of the core centroids. The strength of the secondary-flow vortices was determined by using a circulation criterion on rotated planes aligned to the vortex filaments.

The pressure-side leg of the horseshoe vortex and a second vortex associated with the egress flow were identified by the experimental campaign. In the absence of purge flow the two vortices merged, forming the passage vortex. With the addition of purge flow, the two cores remained independent to 40% of the blade axial chord, while also demonstrating an increased radial migration and intensification of the passage vortex. The egress core was shown to remain closer to the suction-surface with purge flow. Importantly, where the vortex

filaments demonstrated strong radial or tangential components of velocity, the circulation level calculated from axial planes underpredicted the true circulation by up to 50%.

Keywords: Axial Turbine, Secondary Flows, Purge, Volumetric Velocimetry, Vortex Tracking

1 INTRODUCTION

In gas turbine engines, the temperature of the gas entering the high-pressure turbine typically exceeds the safe working limit of the alloys from which the first-stage turbine components are manufactured. Ingress of this hot gas from the annulus into the first-stage rotor-stator wheel-space has the potential to raise the temperature of the highly stressed rotating disc to unwanted levels. Relatively cool air (termed 'purge flow') is bled from the compressor to pressurise the wheel-space and minimise ingress, thereby preventing the rotating disc from overheating. The rotor and stator platforms form a so-called 'rim seal' at the periphery of the wheel-space through which the purge flow egresses into the mainstream gas-path.

It is common practice to model the flow in the mainstream gas-path in the absence of purge flow. The predominant reason for this is to avoid modelling the wheel-space and thereby reduce the size of the computational domain. This approach fails to account for the effect of the interaction between the egress and mainstream flow on the endwall secondary flow field in the blade passage downstream of the rim seal. Endwall secondary flows are a major contributor to overall stage losses; therefore, stage loss predictions obtained from computational models without egress are subject to inaccuracies.

The classical model of secondary flow does not consider egress. The incoming mainstream flow rolls up into the horseshoe vortex at the blade leading edge to form counterrotating legs that bifurcate into adjacent blade passages. The pressure-side leg of the horseshoe vortex (PS-HSV) migrates across towards the suction-side of the neighbouring blade owing to the cross-passage pressure gradient, growing in strength as it entrains crossflow to eventually form the so-called passage vortex. The suction-side leg (SS-HSV) counter-rotates relative to the PS-HSV and PV; it is typically weaker in strength and orbits the PV.

Previously published computational (Schreiner *et al.* [1]) and experimental (Carvalho Figueiredo *et al.* [2]) research conducted at the University of Bath has provided insight into the effect of egress on the classical secondary flow model. It was found that the egress formed its own distinct vortical structure (referred to as the egress vortex, EV) that rotated in the same sense as the PS-HSV. For the vane-blade clocking position simulated in both studies, it was shown that the EV emerged from the rim-seal near to the SS-HSV. Owing to its opposite

sense of rotation and greater strength, it proceeded to overturn the SS-HSV. A schematic showing the key features of secondary flow with egress is provided in Fig. 1.

Qualitative differences in the secondary flow structures that formed with and without the supply of purge flow to the wheel-space were observed by Carvalho Figueiredo et al. [2]. It should be noted that even without the purge flow, there will still be egress from the rim seal owing to disc pumping. Without purge, the EV and PS-HSV merged early in the passage to form the passage vortex; with purge, the EV remained closer to the blade suction surface, which delayed merging with the PS-HSV until later in the passage.
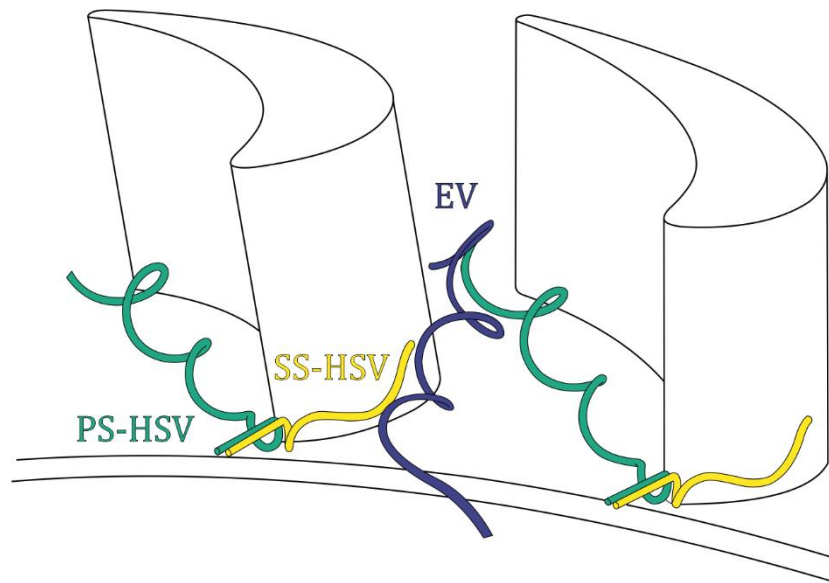
Figure 1: Simplified secondary flow structures in the presence of egress.

The work of Carvalho Figueiredo et al. [2] provided important insight into secondary flow with egress; however, two key questions remain unanswered: first, how does the introduction of purge flow affect the *strength* of the secondary flow vortices; and second, acknowledging that the vortex filaments do not necessarily pass axially through the turbine stage, how does through-passage planar rotation of these filaments affect the assessment of strength and trajectory of the secondary flow vortices? The answers to these questions will advance understanding of the effect of egress on secondary flows and could have implications for the design of the profiles for blades and contoured endwalls.

Section 2 of this paper provides a review of pertinent literature to secondary flows with egress; it also discusses vortex tracking methods. Section 3 outlines a method which can be applied to three-dimensional blade passage velocity fields to determine the strength, core trajectory and merging location of secondary flow vortices. In Section 4 this method is applied to experimentally obtained three-component velocity data in the blade passage

of a turbine operating without purge flow. Finally, in Section 5, the method is used to investigate the effect of purge flow on the behaviour of secondary flows.

2   LITERATURE REVIEW

Section 2.1 provides a brief review of previous investigations that have considered the effect of rim seal egress on secondary flow features in the mainstream turbine annulus. Section 2.2 reviews the salient methods found in the literature related to vortex tracking using Particle Image Velocimetry (PIV) data.

2.1 Secondary Flow Features with Egress

The study of secondary flow structures and their associated impact on turbine stage performance is made challenging by the rotating environment. Researchers must decide whether to use a cascade rig, for which the absence of rotation makes inter-passage measurements relatively straightforward, or a test stage that incorporates rotational effects, but with limited capability to interrogate the inter-blade field. Purge flow can be introduced in both types of rig; however, rotational effects are critical to the appropriate conditioning of the egress flow.

de la Rosa Blanco *et al.* [3] used a linear cascade and five-hole probe pressure measurements taken at 50% of the rotor chord to quantify mixed-out endwall losses. A cavity with tangentially pre-conditioned flow was used to simulate egress through the rim seal. The authors showed that increasing the purge flow rate and tangential velocity strengthened the PS-HSV. The loss cores were shown to radially migrate towards the mid-span and the vortices widened in the pitchwise direction. Mixed-out endwall losses were subsequently increased.

Barigozzi *et al.* [4] studied the effect of rim seal clearance and purge flow rate on secondary flows in a linear cascade. They used variable angle fins to impart a tangential velocity on the egress to simulate rotational effects at the exit of the rim seal. Five-hole probe pressure measurements quantified the passage vortex immediately downstream of the rotor blade. An increase in the purge flow rate was shown to widen the passage vortex core, attributed to the tangential velocity causing a highly negatively skewed inlet boundary layer. This strengthening of the PS-HSV at the higher purge flow rate led to increased secondary flow losses.

Popovic and Hodson [5] used results from a linear cascade to validate a computational fluid dynamics (CFD) model. The predictions and measurements of losses were determined for a range of purge-mainstream mass fractions (MF). Their results showed that the increase of purge flow rate gave rise to a non-linear increase in losses, which could be categorised into three regimes of purge-mainstream interaction. The authors noted that the non-linearity in total losses was due to the variation in the mechanism of purge-mainstream interaction. In the intermediate range of MFs, an unsteady solution was observed due to the periodic filling and emptying of the

outer rim-seal cavity. At high MFs (>1.5%), the purge flow emptied into the passage across the blade pitch, feeding the legs of the HSV and dramatically increasing losses.

As mentioned previously, linear cascades are beneficial in that one may readily make measurements between static "rotor" blades; however, the presence of rotation between stator and rotor fundamentally changes the secondary flow field. This effect was described by Schneider *et al.* [6], who axially-traversed a probe between the rotor and stator rows of a rotating turbine rig. The PV of the upstream nozzle guid vane (NGV) and the resulting shear layer caused unsteady interactions with the rotor secondary flow structures, fundamentally changing the flow field. This study did not incorporate rim-seal flow, which further complicates the blade secondary flow structures.

A large-scale rotating turbine with rim-seal flow was used by Schrewe *et al.* [7] to investigate purge-mainstream interaction. By measuring the temperature difference between the two flows, the authors tracked the trajectory of the purge, showing that the majority became entrained into the PS-HSV. They observed that this intensification caused by the purge flow increased pressure losses and reduced efficiency of the 2-stage turbine. The structure of the secondary flow field and associated loss mechanisms were inferred through probe measurements upstream and downstream of the blade rows; the authors noted general agreement with numerical predictions.

Schuepbach *et al.* [8] studied the effect of purge on the secondary flow structures within a 1.5-stage axial turbine rig. Total pressure measurements from a five-hole probe at the rotor exit plane (axially aligned) identified a low-pressure region associated with the PS-HSV and entrainment of low momentum fluid. Purge flow was shown to increase the size and radial migration of this vortex. While peak vorticity of the passage vortex was reduced with purge flow, the integrated circulation was increased, indicating that the egress had the same rotational direction as the passage vortex and increased its strength. A reduction in efficiency with purge mass flow rate was determined.

Using the same 1.5-stage rotating rig as Schuepbach *et al.*, Regina *et al.* [9] investigated purge flow interactions with the mainstream. A fast-response aerodynamic probe was used to capture the unsteady pressure field at rotor exit and determine the reduction in stage efficiency with purge. The time resolved measurements showed the radial migration of the PS-HSV towards mid-span, which lifted off earlier in the passage when purge flow rate was increased. The authors showed that the reduction in efficiency was greatest near the rotor hub due to the increased strength of the PS-HSV. The secondary flow field was inferred from pressure measurements acquired from axial measurement planes upstream and downstream of the rotor.

In general, cascade measurements afford investigation of the secondary flow structures within the vane and blade passages, albeit with a less representative flow field. Rotating rigs model the rotational effects present in operational engines but prohibit the use of traditional multi-hole probes within the blade passages. Non-invasive optical techniques – such as the Volumetric Velocimetry (VV) employed in this study – are required to interrogate the inter-blade passages and offer insight into the local position and strength of the secondary flow structures.

2.2 Vortex Tracking

For three-dimensional flows, the drawbacks of vorticity-based methods have been realised in that a shear layer cannot be distinguished from a vortex since both could exhibit high vorticity. Indeed, high vorticity is not necessarily an indication of a stronger vortex, as shown in Schuepbach *et al.* [8]. Several vortex identification criteria have therefore been proposed in the literature.

In this paper a vortex core identification parameter, γ_2, has been implemented as a method to track the vortex cores through the blade passage. Graftieaux *et al.* [10] describes γ_2 as a non-localised (Galilean invariant) vortex tracking parameter suitable for PIV data. A key benefit of using γ_2 over alternative parameters such as vorticity is that it is not based on velocity gradients. These gradients amplify any noise in experimental data and often produce poor results when implemented as a vortex tracking tool. It should be noted that Morgan *et al.* [11] also quantified vorticity using the same non-derivative method. Their approach interrogates the region surrounding the local maxima with a size comparable to the vortex core to track the center of gravity.

The application of the non-localised γ_2 parameter was expanded by Simpson *et al.* [12], who used it to identify vortex cores whose vorticity could be integrated to obtain circulation. This study notes that due to the assumption of constant shear within the interrogation region in the calculation of γ_2, the algorithm is less effective for vortices in close proximity to each other. The authors also describe discrepancies in both the strength and position of vortices which do not rotate about the through-plane axis. The inherent problems created by off-axis rotation and vortices in close proximity are particularly applicable for turbomachinery secondary flows.

3   METHODOLOGY

This section introduces the experimental turbine test facility, the optical system employed to conduct VV measurements and the data processing required to interpret the three-dimensional velocity field.

3.1 Mechanical Design

The Large Annulus Rig (LAR) is a single-stage turbine at the University of Bath, designed for advanced optical measurement techniques such as VV. The design and commissioning of the test rig was extensively documented in Jones *et al.* [13] and therefore only a brief overview will be presented here. The VV technique was developed for use in the LAR by Carvalho Figuieredo *et al.* [2]

The mainstream gas-path is fed by a 6-inch pipe, connected to an axial compressor capable of supplying 1.5 kg/s at 2.2 bara. A section of the inlet piping is removable in order to facilitate the retraction of the stator from the rotor (which is fixed axially), to allow for seal changeover and routine maintenance related to the use of seeding oils. The mainstream flow passes through a settling chamber via a conical diffuser, before contracting into the turbine annulus over a nose cone. Baffle plates are installed in the settling chamber to promote mixing of the flow. The mainstream flow is seeded with oil droplets via three inlet ports (shown in purple in Fig. 2). A turbulence grid is installed in the turbine annulus one axial chord upstream of the stator vanes.

Key operating parameters of the test rig are outlined in Table 1; note that two MFs are used in this study.

Table 1: Key operating parameters of the test rig

Parameters	Value	
Disc speed, Ω (rpm)	900	
Rotational Reynolds Number, Re_ϕ	5.9×10^5	
Axial Reynolds Number, Re_w	2.2×10^5	
Flow Coefficient, C_F	0.38	
Vane exit Mach Number, M	0.12	
Degree of Reaction, Λ	0.21	
Blade Loading Coefficient, Ψ	2.2	
Blade Aspect Ratio (= b/c_{ax})	0.73	
Blade Turning Angle (°)	104	
Purge-Mainstream Mass Fraction, MF	0%	1.7%
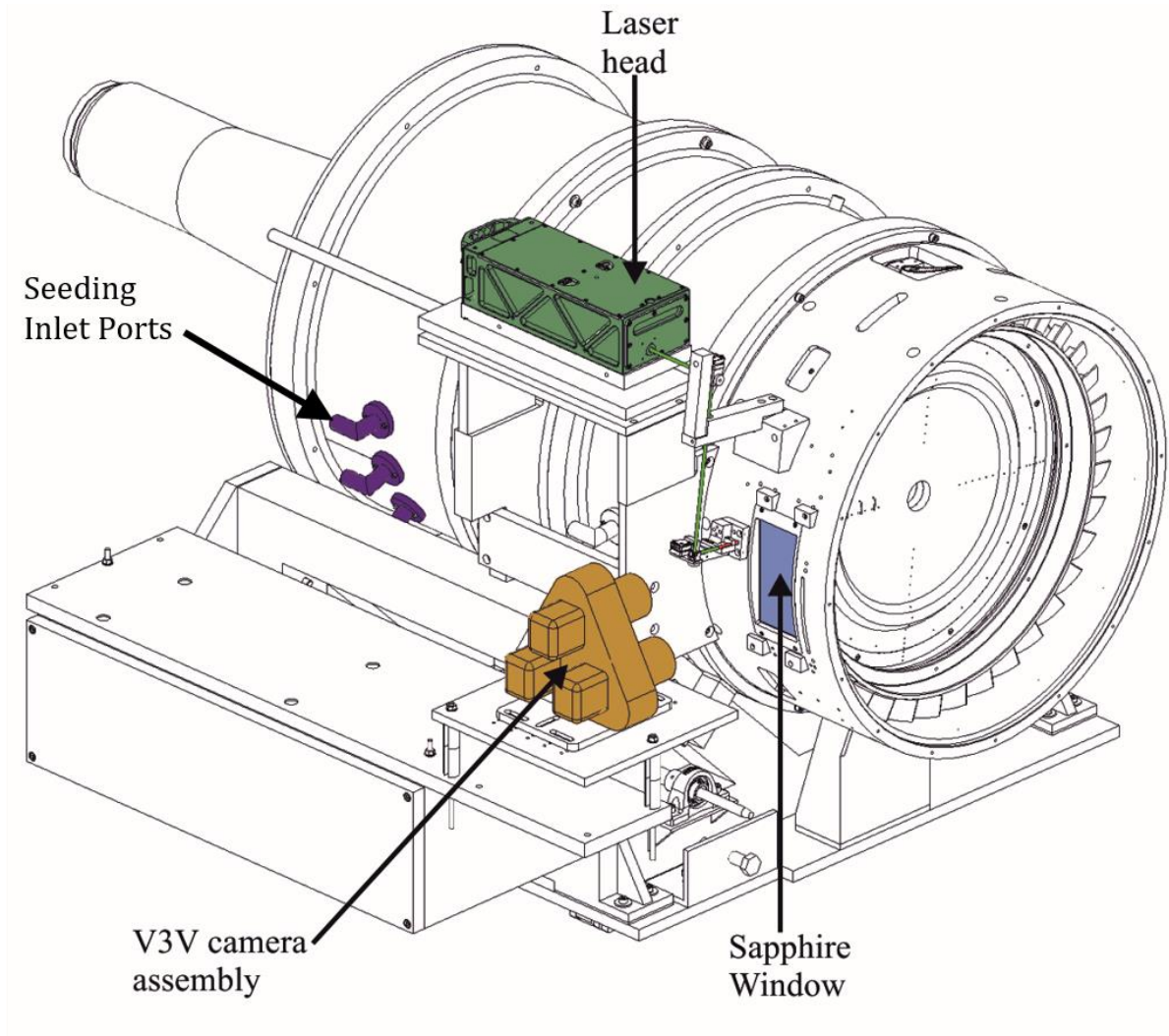
Figure 2: Optically accessible turbine test rig.

The thickness of the turbulent boundary layer was measured upstream of the vane and was determined to be ~20% of the annulus span. A radially-invariant turbulence intensity, σ, of 5% was measured between the boundary layer and the annulus at mid-span. The low aspect ratio blades promote the formation of secondary flows, augmenting these key features within the mainstream flow field.

The seeding medium required for the VV experiments was olive oil, which was atomised as 1μm ø droplets prior to entering the test stage. For oil droplets of 1μm ø, a Stokes number, St, of 0.012 is obtained for the mainstream flow and 0.032 for the purge flow. As this is below an upper limit of 0.1, the particles of this size and substrate will accurately trace the flow to within an error of 1% (Tropea *et al.*[14]). The appropriate seeding level was controlled via a compressed air input to the laskin nozzles in the droplet generators.

The purge flow was supplied at low radius through the bore of the stator disc; ultimately the purge flow was ejected as egress through the double-clearance rim seal (shown in Fig. 3) at the periphery of the wheel-space. The

purge flow-rate was supplied using an 18mm ø tube, fed by a separate compressed air system to the main flow-path. The tube passed through the settling chamber to the machine-axis of the rig via an aerodynamic strut; the strut was designed and implemented to minimise interaction with the mainstream flow, similar to the fairings used in typical gas turbine centre frames. Seeding of the purge flow occurs before entering the test rig and hence the seeding is uniformly mixed by the time it enters the wheel-space.

The 24 stator vanes and 36 rotor blades have profiles based on a current Siemens industrial high-pressure turbine. The vanes and blades are prismatic, *i.e.* there is no taper, lean, twist or sweep. A 3.5 mm fillet exists where the blade and vanes meet the endwalls. The rotor blade tip-clearance with the turbine casing is 0.5 mm. The turned blades generate power, which is absorbed by a dynamometer.

The rotor is modular in design; the blades are made as a single bladed-ring or *bling*. The bling design allows for expedient manufacture and changeover when endwall contouring, rim-seal or blade fillet geometries are to be investigated. The rotor was black anodised to reduce laser reflections.


3.2 Optical Design

VV is a three-dimensional PIV technique which requires access for three cameras, alongside laser access from which to illuminate the seeding particles. A sapphire window in the rotor casing facilitates camera access to the turbine blade passages. The window has a planar outer surface and a curved inner surface with the same radius as the casing.

The VV method employed here is Defocusing Particle Image Velocimetry, branded as V3V by the developer, TSI. This system employs three 8MP CCD cameras mounted within an anti-vibrational bracket that ensures a known position of the cameras relative to the turbine. Three frames are taken at a timestep, $\Delta t = 10\mu s$ apart, resulting in six frames for each data capture.

A Quantel Q-Switch 200 mJ laser is used to illuminate the blade passage through a bespoke optic pathway. From the outlet of the laser, two fused silica prisms rotate the beam through 90 degrees, such that it is aligned with a 6 mm hole in the stator casing. Each prism is attached to a kinematic mount to allow for precise alignment with the hole. The laser enters a borescope, which is removable from the rig, containing two optical components: a lens and a prism. The fused silica concave lens has a negative focal length, causing an expansion of the laser beam into a laser cone. The prism, which has used both fused silica and sapphire as the substrate, rotates the laser cone such that it faces downstream (*i.e.* towards the rotor). The borescope and optical pathway was developed in-

house and is documented in Carvalho Figuereido *et al*. [15,16]; the borescope illumination cone is shown in Fig. 3.
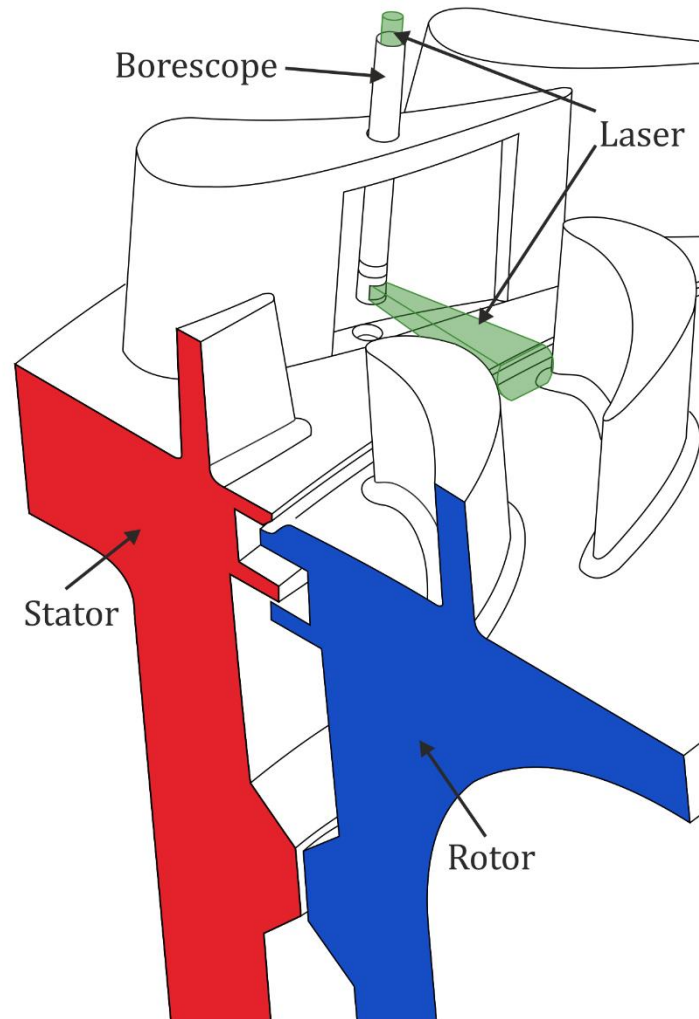
**Figure 3: Turbine Stage Cross-Section with Laser Delivery.**

An optically-transmissive stator vane was designed, manufactured using stereolithography (SLA). The vane features a hollow cavity and is sealed with an NBK-7 plano-convex window. The outer surface of the vane window was designed to imitate the curvature of the vane suction-surface, to within 50μm. The use of a borescope allowed for translation both radially and about the axis of the stem. Translation of the borescope enabled the laser cone to be positioned such that the full extent of the blade passage may be illuminated at a fixed relative rotor-stator position. A recess in the inner radial wall of the optic vane cavity allowed the borescope head to be inserted, thereby enabling the laser cone to be introduced parallel to the endwall, permitting data capture in this key area of interest.

A Compact Instruments VLS7/T rpm optical sensor was installed downstream of the rotor, where the laser was reflected by a marker placed on the rotor disc face. Each VV capture begins at a set delay from the trigger point, determined in order to provide a full view of the passage, corresponding to a clocking angle change of 0.9°; this is consistent for all data presented in this study. The signal from the rpm sensor was output to a TSI 610036 synchroniser, which provided signals to both the cameras and the laser.

3.3 Data Processing

This subsection focuses on the VV process and the analysis of the three-dimensional velocity field required to obtain tracked vortex cores. For general VV calibration processes, the reader is directed towards previous studies published by this group [2,16].

The VV data capture begins with a laser pulse synchronised to the rotor. Three images are initially obtained, followed by a second set at a timestep $\Delta t = 10\mu s$ (*i.e.* six images are captured for each rotor pass). Minimum intensity subtraction, Gaussian filtering and median filtering are used to identify the two- dimensional position of the particles in each of the six images. Within each triplet of images, the particles are matched using the algorithm outlined in Stellmacher and Obermayer [17] to identify three-dimensional positions of the particles at each timestep. This is followed by particle matching between the timesteps to find instantaneous particle velocities, such that the six images have contributed to a single output in a velocity field. The fidelity of this field in isolation is poor, hence an averaging process occurs in which a further 200 repeat sets of six images are obtained to create an ensemble average. Vectors within a 1 x 1 x 1 mm^3 voxel are averaged to contribute to a single output vector. This process is represented in Fig. 4.
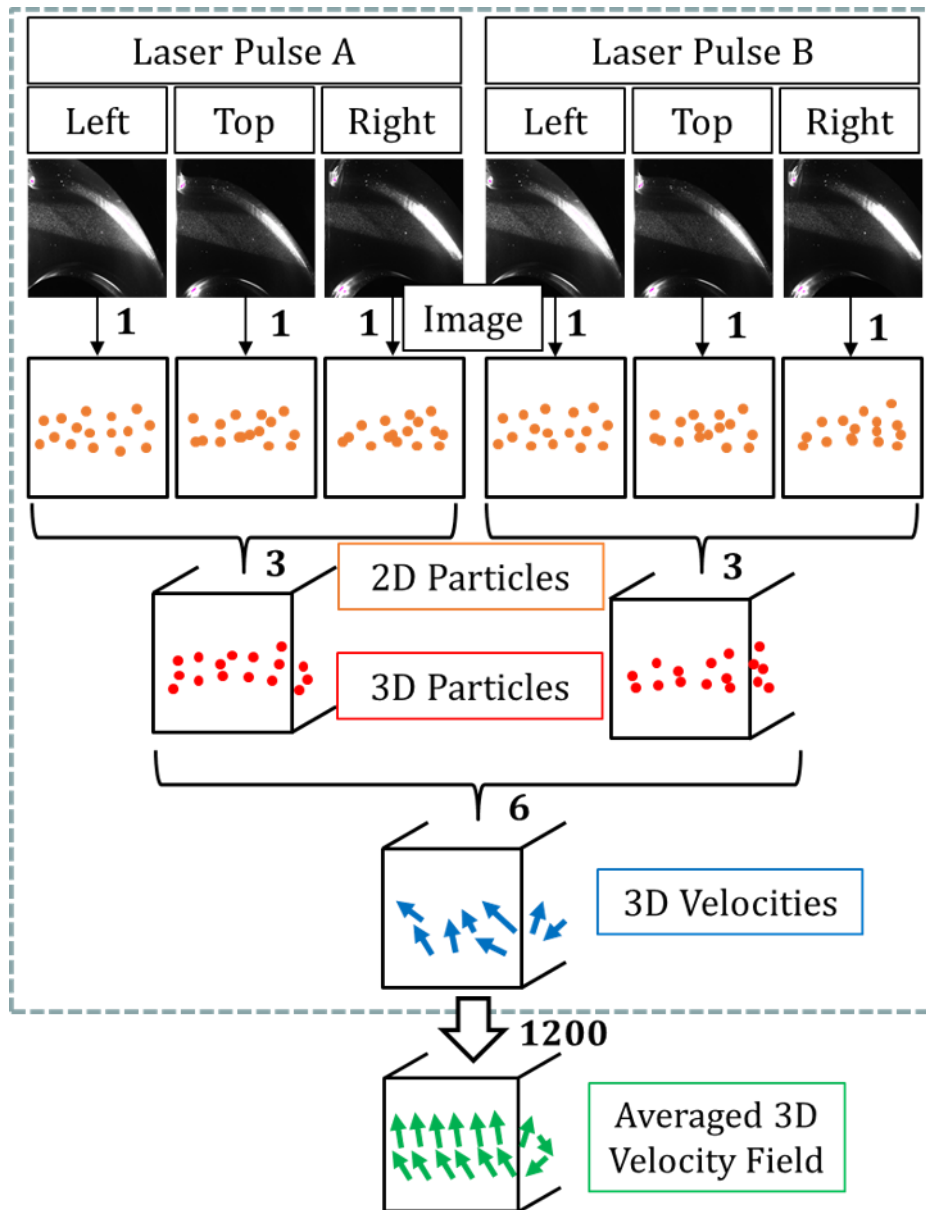
Figure 4: Volumetric Velocimetry Process; steps within the grey, dashed box are repeated 200 times per laser position to create an ensemble average.

A summary of the post-processing structure is provided in Fig. 5. The averaged 3D velocity field (Fig. 5a) is subject to several further filtering and post-processing steps within a MATLAB function. The data must be converted to the camera reference frame - which is calibration-specific due to the short focal length - such that all laser cone positions are in the absolute reference frame (Fig. 5b). Velocity data is filtered (Fig. 5c) to remove voxels (1 mm^3) containing fewer than forty instantaneous vectors; this limit was chosen to prevent spurious data contributing towards a single processed vector. Ghost particles associated with reflections are removed using a

spatial filter in the shape of the blades. A further Median-Average Deviation (MAD) filter was applied to isolate vectors with magnitudes over three times the MAD.
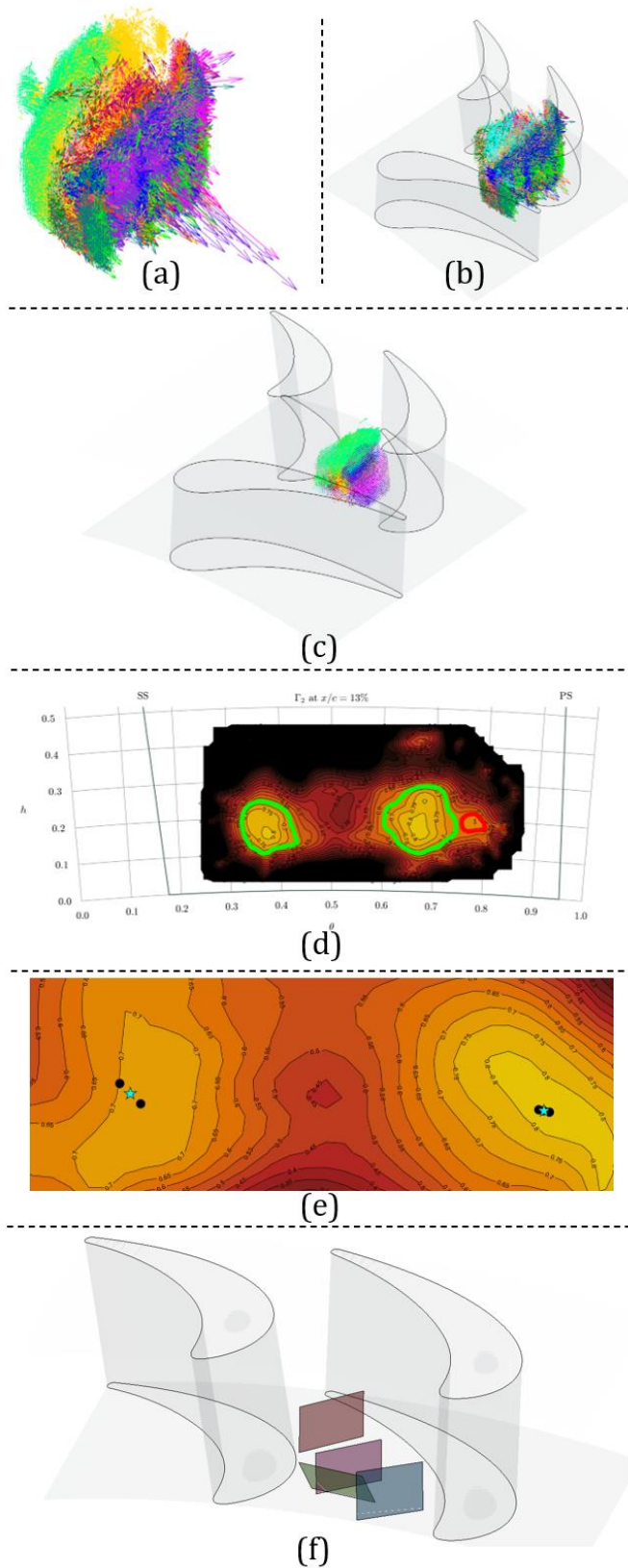
Figure 5: Data Post-Processing Structure.

Given the fixed rotor-stator clocking throughout the experiments, the borescope is translated up to 15 times to illuminate the entire blade passage. Data acquired for different positions of the laser cone were shown to have good overlap in Fig. 6, despite being taken on different days and with independent camera calibrations, highlighting the robustness of the VV method and filtering process. A two-dimensional data set is shown for an arbitrary axial plane, with the vectors coloured to distinguish each laser cone position. Fig. 6 also shows the coordinate system that will be used throughout this study.


(a)

(b)
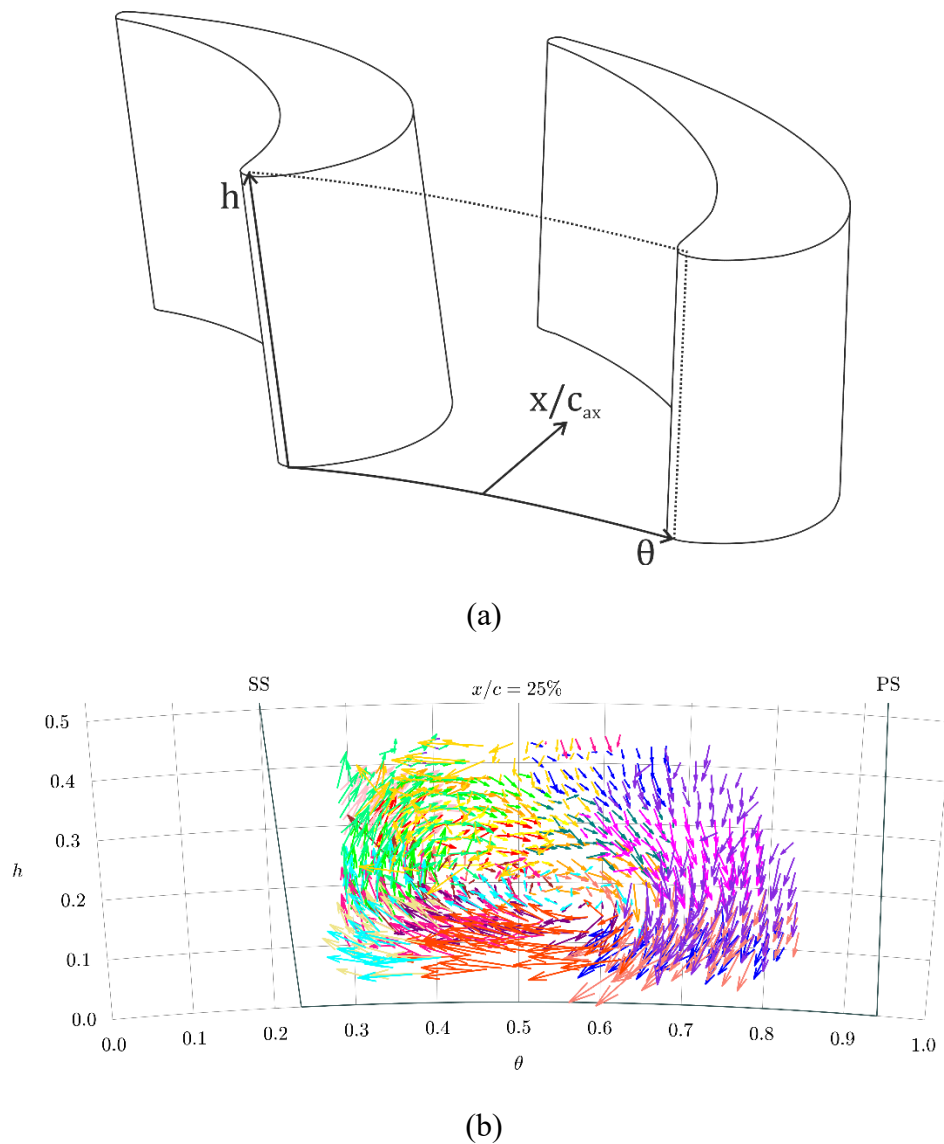
Figure 6: Overlap of data from different laser cone positions: a) Coordinate System; b) Superposed datasets where each colour represents an individual experiment and camera calibration.

A vortex tracking parameter was used to mathematically determine the positions of the vortices. A non-localised method was employed due to the noise amplification issues that can arise when using velocity gradient methods with PIV data. The $\gamma_2(P)$ parameter outlined by Graftieaux *et al.* [10] was implemented, as given in Equations 1 & 2:

$$\gamma_2(P) = \frac{1}{N}\sum_S \frac{\left[\overrightarrow{PM} \times \left(\overrightarrow{V_M} - \overrightarrow{\tilde{V}_P}\right)\right].\vec{n}}{\left\|\overrightarrow{PM}\right\|.\left\|\overrightarrow{V_M} - \overrightarrow{\tilde{V}_P}\right\|} \tag{1}$$

$$\overrightarrow{\tilde{V}_P} = \frac{1}{N}\sum_S \overrightarrow{V_M} \tag{2}$$

These equations have been diagrammatically represented in Fig. 7. Within the interrogation area S, the circulation velocity is determined from all points surrounding the query point P. The size of the area S, in terms of the radius from the point P, may affect the magnitude of the γ_2 parameter, particularly for noisy data as per Morgan *et al.* [11] and Simpson *et al.* [12]. The size of the region S was varied for the data within this study, though no dependence was found. This implies that the filtration of the data was effective at minimising noise.
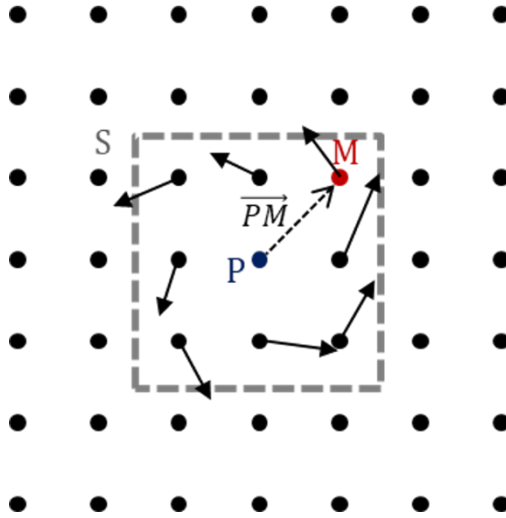
Figure 7: Schematic γ_2 calculation.

Centroids based on isolines of γ_2 were used to determine the positions of the vortex cores (Fig. 5d) as per Morgan *et al.* [11] The variance of the level of γ_2 with the position of the cores will be discussed in Section 4. Centroids of γ_2 were tracked across multiple axial planes to describe the three-dimensional path of the vortices.

The area bound by the isoline of γ_2 was used as the integration area for the summation method of circulation; the strength of the vortices was also determined for each axial plane according to Equation 3:

$$\Gamma = \iint_A \omega \cdot dA = \frac{1}{N} \sum_A \omega \cdot \boldsymbol{n} \qquad (3)$$

where the dA term requires the normal to the plane of measurement, n.

The circulation is multiplied by the area of the isoline-bound region of γ_2 to identify false centroids. Regions with low $\Gamma * A$ are filtered from the dataset, shown in Fig. 5d by the red highlighted lines. The remaining cores across multiple isoline γ_2 levels are subject to cluster analysis to identify the true core position of the vortices (Fig. 5e). The number of cores may be tracked across multiple axial planes, and if only one core is repeatedly identified, the cores are taken to have merged and formed the passage vortex.

With three-dimensional components of vorticity available through use of the VV method, it is possible to rotate the plane of measurement in order to obtain a more accurate circulation for the vortices (Fig. 5f). By aligning the plane of measurement to the direction of travel of each vortex filament (determined by the centroid tracking approach), a maximum value of circulation will be obtained. The impact of plane rotation is discussed in Section 4.

3.4 Uncertainty Analysis

The width of a CCD pixel is 5.5 μm. With a nominal magnification of 0.24, each pixel covers a region of length 23 μm. Camera calibration determined a least-squares error of 12 μm, approximately half a pixel. This translates to an in-plane displacement uncertainty, Δx and Δy of ±0.5 pixels. The uncertainty of through-plane displacement, Δz, was scaled by triangulation of the particle triplet to ±2 pixels.

Reference values for the calculation of absolute uncertainty in velocity magnitude were calculated using absolute average velocity components of all data. These were determined to be $u = 13.2$ ms^{-1}, $v = 30.1$ ms^{-1}, $w = 4.0$ ms^{-1}. The absolute uncertainty in velocity magnitude was determined using the equation in Carvalho Figueiredo *et al.* [16]. In addition to the displacement uncertainty above, the equation requires a temporal uncertainty. The laser pulse has a timestep $\Delta t = 10$μs with an uncertainty of ±7 ns limited by the half-width-half-maximum. The uncertainty in velocity magnitude was determined to be 1.2 ms^{-1} or ± 3.7%.

The uncertainty in positioning of the vector is influenced by errors in synchronisation with the rotor, approximately ± 1 μm. This is negligible given the orders of magnitude difference between the velocity vector and the positional error.

4   BASELINE FLOW FIELD

This section presents the vortex tracking and circulation measurements for the baseline case, *i.e.*, no purge flow. The baseline case is presented first because the merging of the egress vortex and the PS-HSV to form the passage vortex occurs earlier in the passage (as identified by Carvalho Figueireido *et al.* [2]), which allows for the methods of vortex tracking and determining the strength of the structures to be applied to both the unmerged and merged vortices. Indeed, the data presented here is an extension of the measurements of Carvalho Figueireido *et al.* [2] with extra volumes at higher radial extent, above $h = 0.3$, to enable vortex tracking as they lift off the hub when merging occurs. The baseline and purge flow cases are then compared in Section 5.

4.1 Two-dimensional fields

Despite the three-dimensional nature of the dataset, it is easier to interpret as two-dimensional planes. The full data set covers a volume that extends between $0.05 < h < 0.40$ and $0.01 < x/c_{ax} < 0.45$. Fig. 8 presents axial planes at $x/c_{ax} = 0.05$, 0.15, 0.25 and 0.35 to illustrate the methods and general trends. The rows denote increasing axial distance; the columns illustrate three different presentations of the same data. The left column is vectors coloured according to velocity magnitude, normalised by the rotor relative velocity vector, V_2, obtained from the isentropic velocity triangles. The middle column shows the same vectors, monochromatically on a contour of the corresponding γ_2 field. The right column reproduces the γ_2 field, with isolines of $\gamma_2 = 0.65$ superimposed to highlight the areas used for determining the circulation integration area and the centroids used to estimate the vortex cores, indicated by star symbols. An ideal Lamb-Oseen vortex has an inner core bound by $\gamma_2 = 2/\pi$ [10] hence the use of isolines of $\gamma_2 = 0.65$.

At $x/c_{ax} = 0.05$ coherent vortical structures are difficult to discern in the raw vector field although some rotation is observed. The γ_2 contours show increased levels indicating the existence of vortical structures. A centroid can therefore be determined although its location at this x/c_{ax} is very sensitive to the isoline level used for the centroid detection due to differences in the strength of the egress and PS-HSV cores.

At $x/c_{ax} = 0.15$ the two vortices are more distinct and discernible even in the vector field. The centroids have moved closer together, primarily due to the PS-HSV moving towards the suction-side of the adjacent blade. The centroids show poor alignment with the visually established centre of rotation in the raw vectors. The cause is shown in the right-hand side column, where multiple isolines of $\gamma_2 = 0.65$ have been detected. The γ_2 parameter is affected by the presence of vortices in close proximity to each other. As outlined by Simpson *et al.* [12], the assumption of a constant circulation velocity $\vec{V}_p$ within the region S of the γ_2 calculation requires constant shear

within the region *S*, which is not true for vortices in close proximity. This results in the lack of a true core defined by a single isoline position, analysis of which will follow in Section 4.2.

Moving aft to $x/c_{ax} = 0.25$ and 0.35, the vortices have merged to form the passage vortex, characterised by a single strong core of γ_2, and a centroid that closely matches the apparent centre of the vortex. Comparison of the two axial planes shows the passage vortex moving radially outward and toward the suction-surface as it progresses through the blade passage.

4.2 Three-dimensional vortex tracking

To establish the vortex path through the blade passage it is necessary to establish centroids of γ_2 in all axial planes. There is therefore a dependence of the vortex core location on the level of γ_2 selected for the isoline which will influence the resultant path. To demonstrate this sensitivity, Fig. 9 shows all centroids of γ_2 plotted on the same cascade view of the passage. The γ_2 value is represented through greyscale with dark equating to $\gamma_2 = 0.75$ and the lightest grey equating to $\gamma_2 = 0.5$ with intervals of 0.05 between.
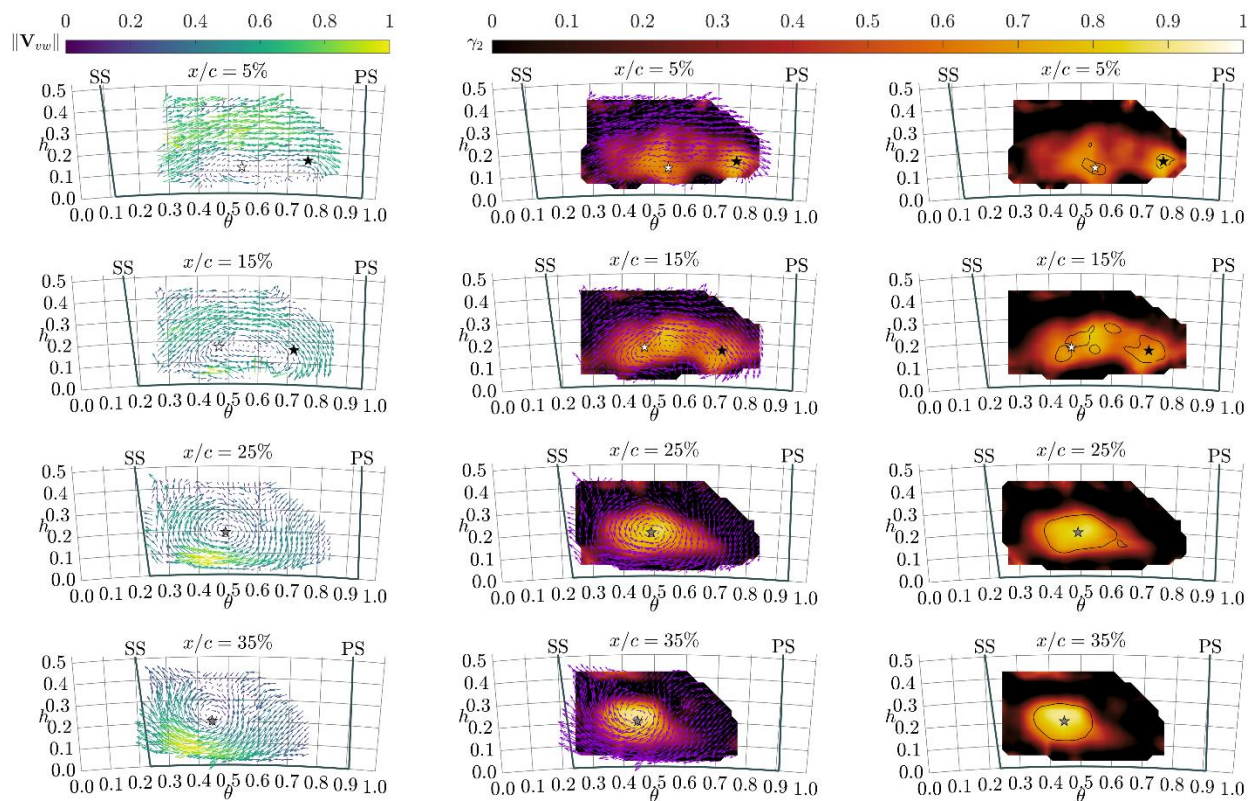
Figure 8: L-R; in-plane velocity vectors coloured by normalised magnitude; monochrome vectors upon a field of γ_2; γ_2 field annotated with isolines of $\gamma_2 = 0.65$. All plots show centroids of γ_2. T-B; axial planes at $x/c_{ax} = 0.05$, 0.15, 0.25 and 0.35.

As previously stated, an ideal Lamb-Oseen vortex has an inner core bound by $\gamma_2 = 2/\pi$ [10]. However, a real vortex or system of vortices is more complex with shear layers and merging processes. This results in a sensitivity of the vortex core position on the selected isoline-level. This section will investigate this sensitivity for the EV PS-HSV merging process to determine an appropriate level for this non-ideal case.

The lower values of γ_2 isoline ($< 2/\pi$) clearly display noise and erroneous results. For example, the cores found closest to the edge of the data are non-physical peaks associated with clipping at the boundaries. These non-physical "cores" may be eliminated using a filter to remove those with low $A*\Gamma$. The area, A, being that bounded by the isoline of γ_2, as shown by the black lines on the plots in the right-hand column of Fig. 8. This parameter is used as it eliminates both small areas of high γ_2 and large areas with low γ_2 alike. Both are indicative of false positives. Either parameter in isolation would not be sufficient to remove these two error cases and could lead to false elimination of true cores.

The in-plane vectors indicate two cores early in the passage, merging to one core around $x/c_{ax} \approx 0.20$. The core closest to the pressure-side, the PS-HSV is well defined particularly for high γ_2 levels and can be seen travelling towards the suction-side. The only isoline-level to correctly detect the merging process is $\gamma_2 = 0.75$. This shows the core rapidly merging with the egress core between $x/c_{ax} = 0.18$ and 0.20.

Ignoring the false cores at the edge of the data, all isoline-levels accurately detect the single passage vortex. Towards the end of the measurement region $x/c_{ax} > 0.4$, further centroids are detected although it is unclear as to whether these are physical, due to the changing nature of the passage vortex causing a more diffuse core, or are non-physical, due to greater noise at the extremities of the measurement region. The laser enters from left to right in the cascade view, hence the laser power diminishes as it progresses through the passage.

The egress core is not as well defined. The medium to high range isoline-levels show a range of core locations on each plane early in the passage, at $\theta \sim 0.5$. These multiple centroids are linked back to those seen in the early planes in Fig. 8. This problem is due in part to the relatively weak egress core, which is only formed from the continuity of flow through the rim-seal. For very low isoline-levels in the early passage ($x/c_{ax} < 0.15$), the isoline envelopes both cores, and hence the centroid shifts to the middle of the two cores, indicated by the darker symbols at $\theta \sim 0.6$. This result is useful in that it can be used as an indication as to when the cores are merged through comparison of isoline levels.

Fig. 9 demonstrates the sensitivity of selecting an appropriate γ_2 level for centroid determination. Merging behaviour and the exact position of the vortices may be masked by incorrect choices at this stage of the analysis. The lowest isoline-values clearly do not capture the vortex locations accurately so can be eliminated. However,

even with the higher isoline-levels there is not a single value that gives a good, consistent, result. The best results have been found through using a range of the higher isoline-levels with the lower values as logical operators to determine merging behaviour and for finding the true centroid of the weaker egress core.

The proposed solution to this problem is to use multiple isoline-levels in the range 0.65-0.75 to define a cluster of centroids in which the core is located. The centroid of this cluster, itself made up of multiple centroids, may be used to illustrate the movement of the vortex core. This solution when applied is shown as blue stars in Fig. 9 and is subsequently applied to both datasets in Section 5.1, with reference to the secondary flow structures.
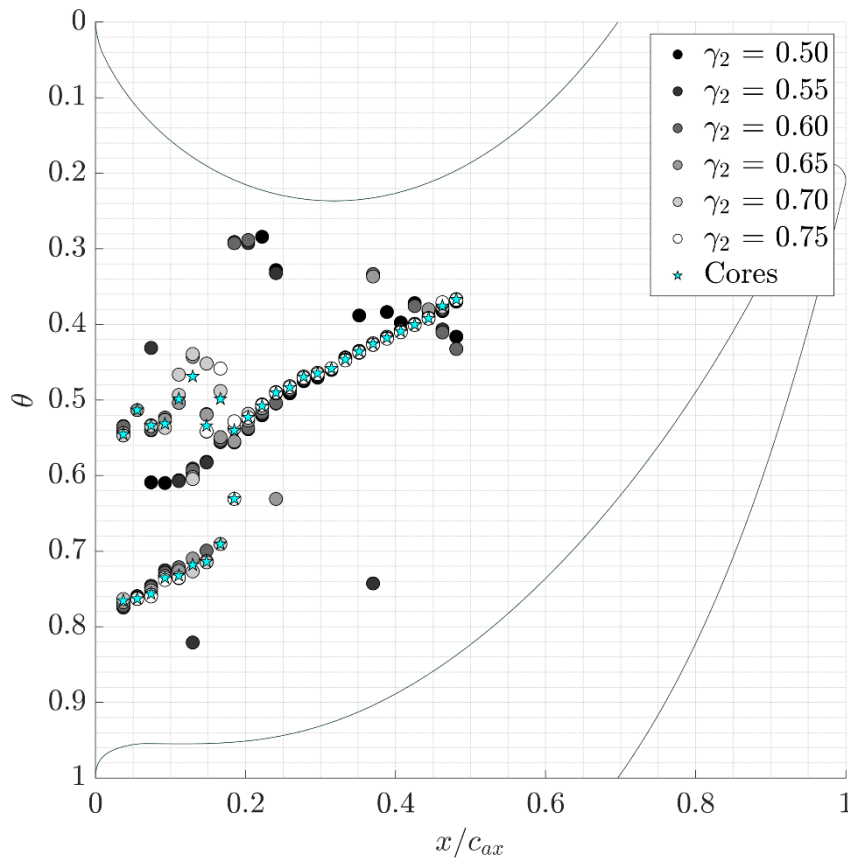

Figure 9: Cascade view of blade passage with γ₂ centroids; dark = 0.5, light = 0.75, increasing in intervals of 0.05. Stars represent vortex cores determined through filtering of centroids.

4.3 Circulation with off-axis rotation

Vorticity alone does not denote vortex strength and must be integrated over an area to determine circulation, as demonstrated by Schuepbach *et al.* [8]. Equation 3 may be used to determine the circulation of the vortices. The area A is that bound by the isoline at a given γ_2 isoline-level. However, in studies outlined in the literature review [11, 12] it was found that the area S should be perpendicular to the axis of rotation of the vortex. From the tracking in Fig. 9 the vortex filaments are not aligned with the axial direction for any case implying that the axis of rotation is not aligned correctly. Thus, it is necessary to rotate the two-dimensional plane such that the

normal to the plane is the axis of rotation. Fig. 10 demonstrates the effect of planar rotation on the strength of the PS-HSV. The carpet plot was generated using spherical linear interpolation to rotate the plane given the user defined maximum bounds of rotation.
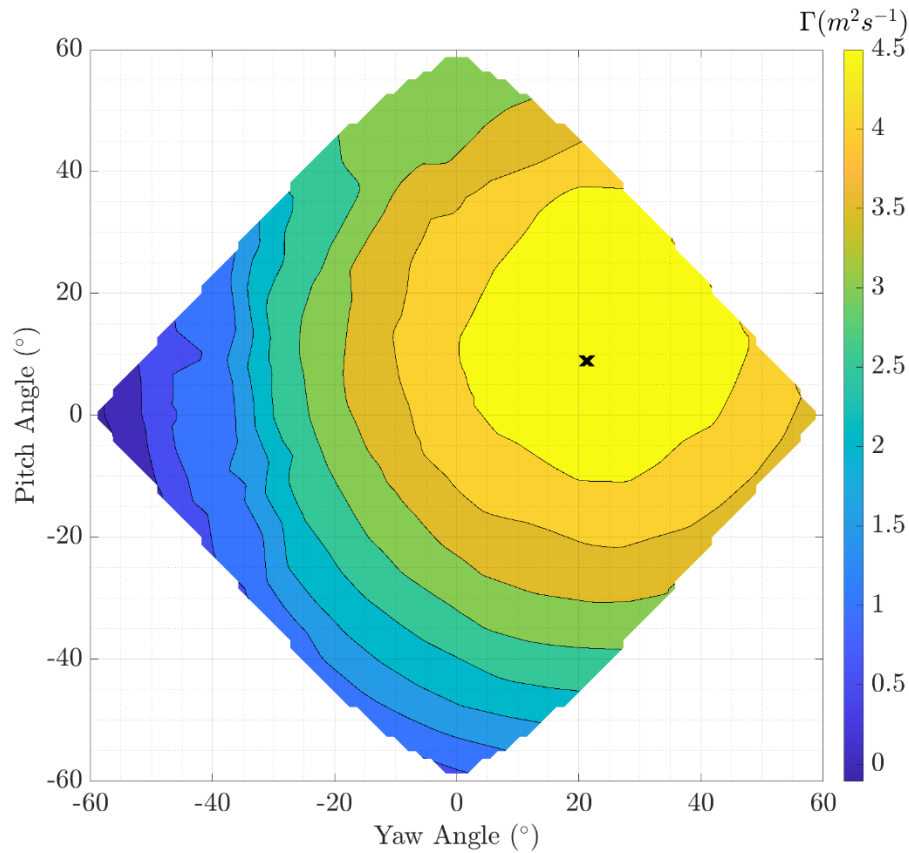

Figure 10: Variation of circulation with yaw and pitch angles for *x/c*$_{ax}$ =35%, with the maximum circulation indicated with a cross.

Fig. 10 is used to highlight some key features of planar rotation on vortex strength. The circulation obtained from the arbitrary axial plane where pitch and yaw are zero is 4.41 m^{2}s^{-1}. By rotating the plane to 21° in yaw and 9° in pitch, a maximum circulation is obtained as 4.98 m^{2}s^{-1}, or 13% larger than the axial case; for certain axial planes this increase was up to 50%. This large deviation suggests an underprediction of secondary flow strength in typical turbomachinery studies which use axial planes as standard. The rotation of the resulting plane is similar to the angle obtained from the tracking using the centroids on axial planes; that is the merged vortex is moving upwards and to the right. The angle of the maximum circulation plane is shown for three example axial locations in a three-dimensional view of the passage with an isosurface of $\gamma_2 = 0.65$ in Fig. 11.

In the early passage, where the vortices are independent, the yaw angle of the planes of maximum circulation for the PS-HSV (in black) and the EV (in green) show that they are moving toward each other. Each of the three planes in Fig. 11 have small pitch angle, which is greatest for the EV in the early passage, indicative of the upward

movement of the core as it emerges from the rim seal. The red plane for the PV shows good alignment of the maximum circulation plane with the isosurface of γ_2.
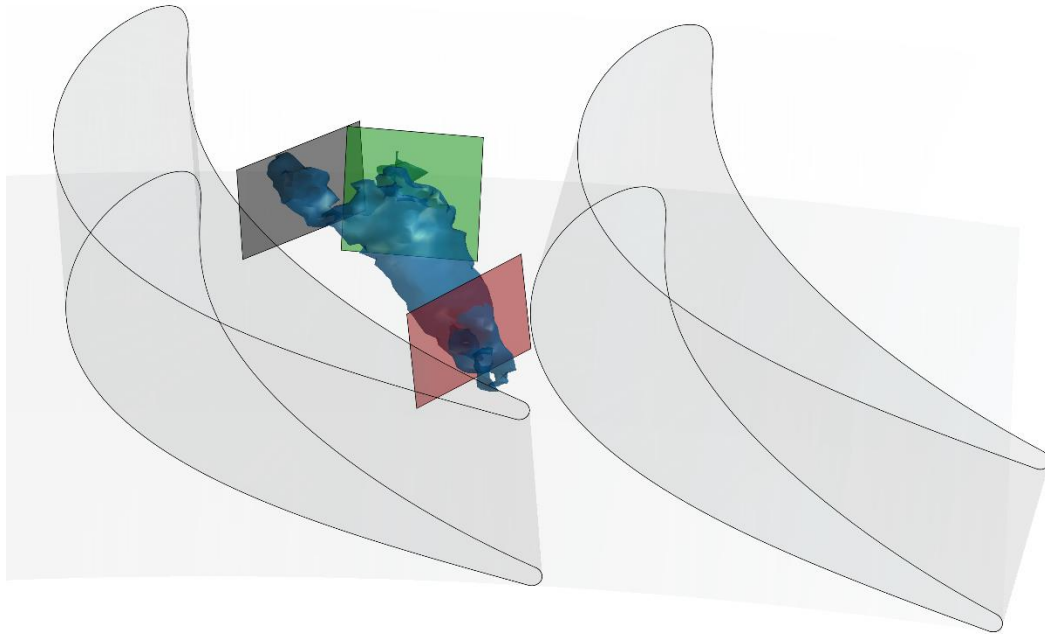

Figure 11: Isosurface of $\gamma_2 = 0.65$ in blue. Planes aligned with vortex filament for; PS-HSV at x/c_{ax} =11%, black; EV at x/c_{ax} =11%, green; PV at x/c_{ax} = 48%, red.

5   PURGE-MAINSTREAM INTERACTION

This section compares the results for the 0% MF and 1.7% MF test cases. The results were processed using the methodology outlined in Section 4.

5.1 Vortex Tracking

The left and right columns of Fig. 12 plot the through-passage trajectory of the egress vortex and PS-HSV for the 0% MF and 1.7% MF cases respectively. White symbols indicate the position of the egress vortex core; black symbols indicate the position of the PS-HSV core. Considering the studies outlined in the literature review, the existence of an egress vortex is only confirmed by measurements within the blade passage; downstream of the blade row the egress vortex has been subsumed by the passage vortex and is unidentifiable. The core of the passage vortex – which is formed when the egress vortex and PS-HSV merge – is represented by grey symbols. The bottom row of Fig. 12 shows the three-dimensional path of the vortex cores; the middle and upper rows show the equivalent path in the meridional and cascade views respectively.
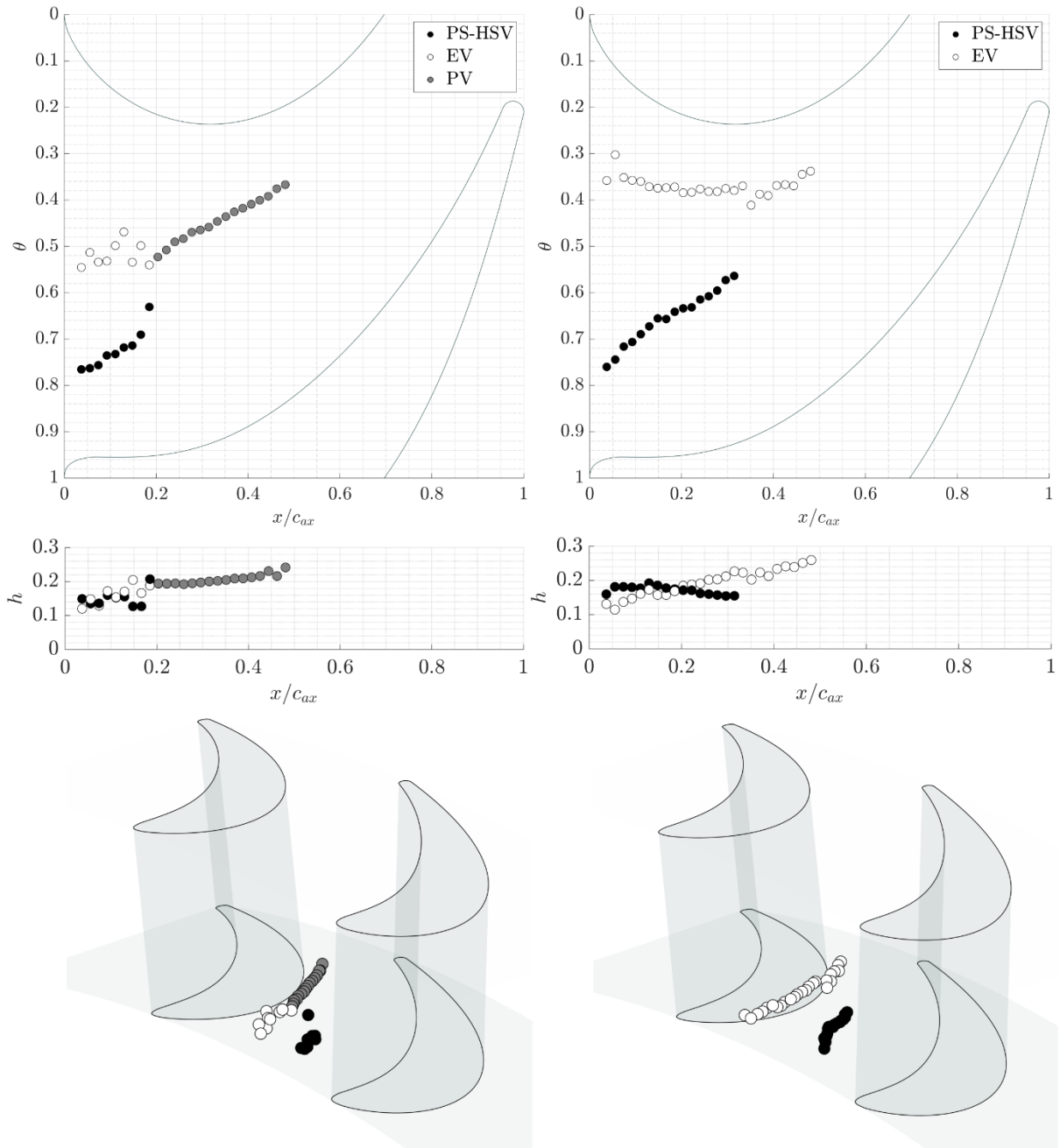
Figure 12: Vortex tracking in cascade, meridional and three- dimensional views from top to bottom. Left: 0% MF; Right, 1.7% MF. Symbols are coloured: white - egress core; black - HSV-PS; grey - passage vortex.

It should be noted that for the 1.7% MF case there is no data plotted for the PS-HSV core beyond $x/c_{ax} = 0.35$. This is because a portion of the PS-HSV became excessively wall-bound, existing within an area of prohibitively high laser reflections; as such, it was not possible to accurately predict the path that the core took in subsequent axial planes.

It is apparent from Fig. 12 that for both MF cases, the cores of the egress vortex and PS-HSV are distinguishable early in the blade passage ($x/c_{ax} < 0.2$). The PS-HSV core enters the passage at a similar pitchwise location in both instances ($\theta \sim 0.85$); however, there is a marked difference in the location at which the egress vortex enters. Without purge, the egress vortex enters in the centre of the blade passage ($\theta \sim 0.5$). For the 1.7% MF, the egress vortex enters the passage significantly closer to the SS of the blade; it then tracks the SS of the blade as it flows through the passage.

The 0% MF results show that the egress vortex merges with the PS-HSV at $x/c_{ax} \sim 0.2$ and forms the passage vortex. Entrainment of egress into the PS-HSV was observed by Schrewe *et al.* [7]. Coalescence of the egress vortex and PS-HSV was not observed for 1.7% MF, with distinct cores evident throughout the measurement volume. In the 1.7% MF case, the PS-HSV moves towards the hub as it flows through the blade passage – this behaviour was also observed in supporting CFD simulations [1]. The CFD results showed that the PS-HSV moves towards the hub and eventually 'undercuts' the egress vortex. In the experiments, the movement of the PS-HSV towards the hub resulted in the vortex progressively moving outside of the illumination region as it flowed through the blade passage, as discussed above. This resulted in missing velocity vectors, which meant that it was not possible to accurately track the PS-HSV beyond $x/c_{ax} = 0.35$. Accordingly, the undercutting of the egress vortex by the PS-HSV was not explicitly observed in the experiments; however, the movement of the PS-HSV towards the hub co-insides with an uplift in the egress vortex – this suggests that the PS-HSV moves under the egress vortex, thereby forcing it upwards.

At the downstream limit of the measurement volume ($x/c_{ax} \sim 0.45$), the radial extent of the secondary flow is marginally increased for the 1.7% MF case; this is consistent with the findings of Schuepbach *et al.* [8] and Regina *et al.* [9]. The radial extent of the core of the passage vortex is <25% of the annulus height for 0% MF whereas the core of the egress vortex is >25% of the annulus height for 1.7% MF. This further supports the notion that there is an undercut of the egress vortex by the PS-HSV in the 1.7% MF case that forces the radially outward movement of the egress vortex.

5.2 Vortex Strength

The distribution of circulation through the passage at a single γ_2 isoline level of 0.65 is given in Fig. 13. This limit was chosen as it allows for an area to be defined on each plane where higher γ_2 levels are not found. The comparison of the circulation is also halted at $x/c_{ax} = 35\%$ for the PS-HSV in the 1.7% MF case due to the radial extent being lower than the measurement volume.
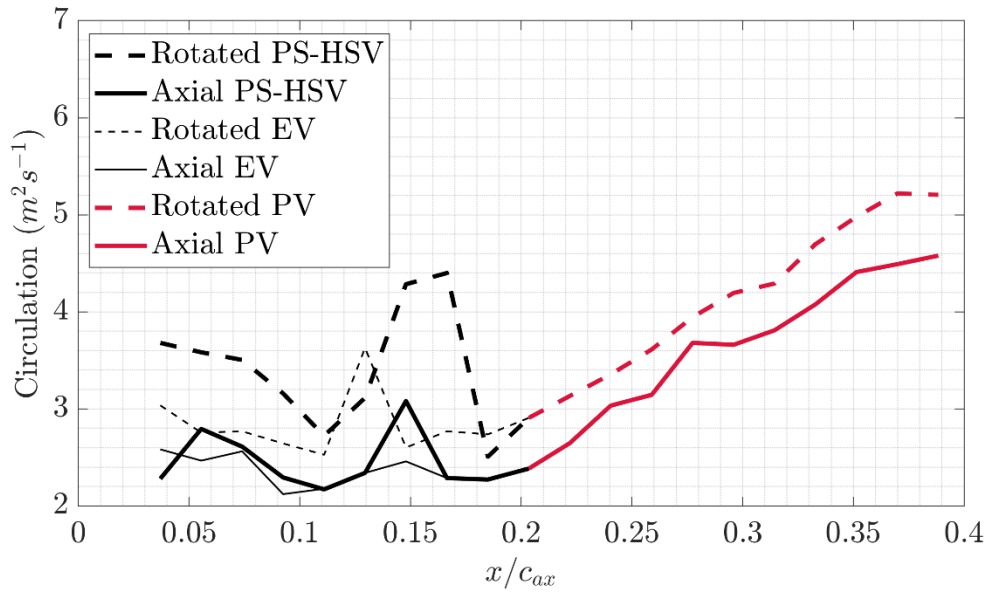
(a)
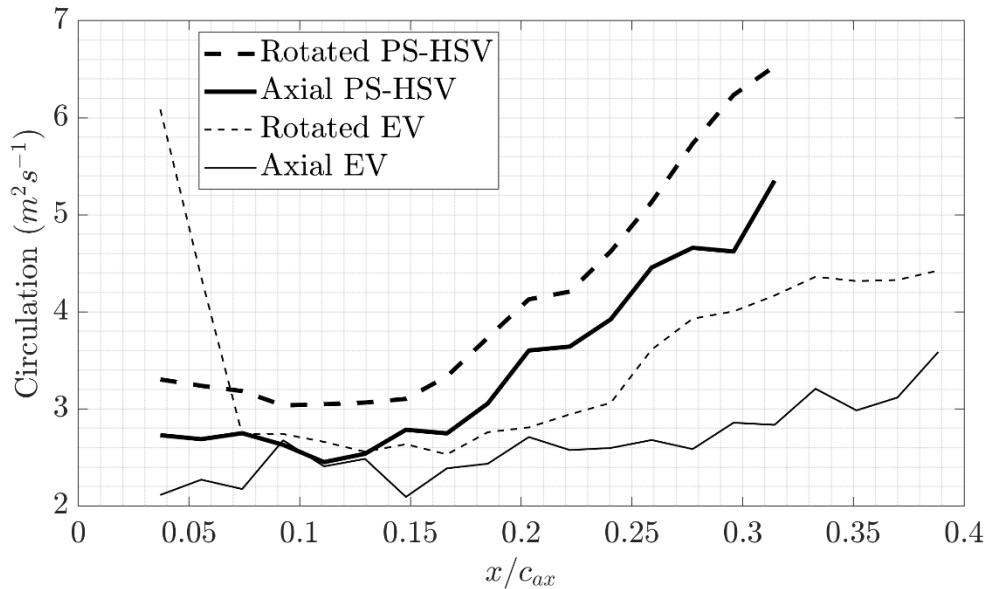
(b)

Figure 13: Circulation distribution in the passage: (a) 0% MF, (b) 1.7% MF.

In Fig. 13 the solid lines represent the circulation as calculated from the axial planes; dashed lines represent the maximum circulation determined from the planes rotated in pitch and yaw. At all axial positions the circulation for the rotated planes are significantly greater than for the axial planes. This indicates that the vortex filaments are not perpendicular to the axial planes. Importantly, where the vortex filaments have strong radial or tangential components of velocity the circulation level calculated from the axial planes may underpredict the true circulation

by up to 50%. This difference is particularly evident at $x/c_{ax} = 0.05$-0.1, where the egress vortex is ejected radially from the rim-seal clearance. A similar effect can be seen for the 1.7% MF case at $x/c_{ax} > 0.25$.

For 0% MF, the circulation remains approximately constant for both the egress vortex and PS-HSV until they coalesce to form the passage vortex at $x/c_{ax} = 0.2$. Subsequent entrainment of the crossflow into the passage vortex leads to a steady increase in circulation from 2.91 m^2s^{-1} to 5.22 m^2s^{-1} as it moves through the passage – this is consistent with classical secondary flow theory.

For the 1.7% case, HSV-PS strengthens from 3.30 m^2s^{-1} in the early passage to > 6.53 m^2s^{-1} at 35% axial chord; the egress vortex also gains strength, increasing from 2.74 m^2s^{-1} to 4.36 m^2s^{-1}. Interestingly, the strength of the egress vortex in the early passage is similar for both MF cases. In earlier work by Carvalho Figueiredo [2], it was suggested that purge *strengthened* the egress core, although in the absence of any quantifiable vorticity parameter conclusions were drawn solely from contours of γ_2. Nonetheless, the work presented here, which directly quantifies vortex strength through circulation, shows that that egress core remains broadly similar in strength early on in the passage; however, it increases in circulation after $x/c_{ax} \sim 0.2$.

Carvalho Figueiredo *et al.* [2] also postulated that the passage vortex was intensified with purge flow, while it was also suggested to form (from the coalescence of the PS-HSV and the EV) deeper into the blade passage. This conclusion is substantiated here through direct assessment of the circulation levels at $x/c_{ax} > 0.2$. It is evident that the inevitable merging of the PS-HSV and the EV in the case with purge flow occurs at $x/c_{ax} > 0.4$; the circulation levels at $x/c_{ax} = 0.3$ far exceed the levels for the 0% MF case.

The subtleties drawn out from appropriate assessment of vortex strength (namely a quantifiable criterion and integration plane perpendicular to the vortex filament) demonstrate the importance of the work presented in this paper. It is hoped that other researchers and designers may consider this when assessing secondary flow features using axial planes and qualitative interrogation methods.

6   CONCLUSIONS

This study employs Volumetric Velocimetry (VV) to accurately capture three-dimensional secondary flow features in an optically-accessible turbine test stage. VV data is presented for cases in the presence and absence of purge flow in order to investigate the purge-mainstream interaction phenomena. Vortex tracking algorithms were applied to the velocity field in order to discern the individual vortical structures.

The vortex tracking parameter γ_2 was used to determine centroids based on isolines in two-dimensional axial planes. The level of γ_2 used in the centroid calculation caused variance in the position of the centroids, hence a

weighted approach was implemented to remove those with low $A*\Gamma$. The refined area bound by the isoline of γ_2 was used to calculate the circulation for independent vortical structures. Spherical linear interpolation was used to rotate the two-dimensional plane such that the normal to the plane is the axis of rotation (*i.e.* perpendicular to the vortex filament). In turbomachinery, the secondary flow vortices travel significantly deviant from the axial direction; data in this study using axial planes underpredicted vortex strength by up to 50%.

The vortex tracking and strength quantification analysis was applied to two datasets: 0% and 1.7% purge-mainstream mass fractions. The quantifiable position of the cores showed increased radial migration of the secondary flow structures with purge, with the enhanced egress core travelling in close proximity to the blade suction-surface. Without purge the PS-HSV and egress core were shown to merge and form the passage vortex at $x/c_{ax} \sim 0.2$; no merging was seen in the case with purge, where two independent vortical structures remained at $x/c_{ax} \sim 0.4$. With purge the PS-HSV was seen to pass underneath the egress core during its cross-passage migration, corroborating numerical predictions. The circulation levels at $x/c_{ax} = 0.3$ exceeded the levels for the no purge case and provide substantiating evidence that the egress core and PS-HSV are strengthened with purge.

ACKNOWLEDGEMENTS

Data access: due to confidentiality agreements with research collaborators, supporting data can only be made available to *bona fide* researchers subject to a non-disclosure agreement. Details of how to request access are available at the University of Bath data archive[1].

Acronyms

CCD	Charged Couple Device
CFD	Computational Fluid Dynamics
EV	Egress Vortex
HSV	Horseshoe Vortex
LAR	Large Annulus Rig
MAD	Median-Average Deviation

---

[1] http://dx.doi.org/10.15125/BATH-00116

NGV	Nozzle Guide Vane
PIV	Particle Image Velocimetry
PS	Pressure-Side
PV	Passage Vortex
SLA	Stereolithography
SS	Suction-Side
VV	Volumetric Velocimetry

Symbols

A	Integration Area for Γ (m^2)
b	Blade Span (= 39.5 mm)
c_{ax}	Axial Chord (= 54 mm)
C_F	Flow Coefficient (= Re_w / Re_ϕ)
h	Dimensionless Spanwise Coordinate
M	Vane exit Mach number
MF	Purge-Mainstream Mass Fraction
$\vec{n}$	Normal Vector
$\overrightarrow{PM}$	Radius Vector
Re_w	Axial Reynolds Number
Re_ϕ	Rotational Reynolds Number
S	Interrogation Area for γ_2 (m^2)
St	Stokes Number
$\overrightarrow{V_M}$	Velocity Vector
$\overrightarrow{V_P}$	Local Convection Velocity Vector
V_2	Bulk Relative Mainstream Velocity
x	Axial Coordinate (m)
Γ	Circulation (m^{2}s^{-1})
γ_2	Vortex Identification Parameter
Δt	Laser-pulse timestep (s)

θ	Dimensionless Pitchwise Coordinate
Λ	Degree of Reaction
Ω	Disc Speed (rpm)
ω	Vorticity (s^{-1})

REFERENCES

[1] Schreiner, B. D. J., Wilson, M., Li, Y. S., and Sangan, C. M., 2020, "Effect of Purge on the Secondary Flow-Field of a Gas Turbine Blade-Row." ASME. Journal of Turbomachinery, 142(10), 101006

[2] Carvalho Figueiredo, A. J., Schreiner, B. D. J., Mesny, A. W., Pountney, O. J., Scobie, J. A., Li, Y. S., Cleaver, D. J., Sangan, C. M., 2021, "Volumetric Velocimetry Measurements of Purge-Mainstream Interaction in a 1-Stage Turbine", ASME. Journal of Turbomachinery, 143(4): 041011.

[3] de la Rosa Blanco, E., Hodson, H.P., and Vazquez, R., 2009, "Effect of the Leakage Flows and the Upstream Platform Geometry on the Endwall Flows of a Turbine Cascade," ASME. Journal of Turbomachinery, 131(1), 011004.

[4] Barigozzi, G., Franchini, G., Perdichizzi, A., Maritano, M., and Abram, R., 2013, "Purge flow and interface gap geometry influence on the aero-thermal performance of a rotor blade cascade," International Journal of Heat and Fluid Flow, 44, pp. 563-575.

[5] Popovic, I. and Hodson, H. P., 2013, "Aerothermal Impact of the Interaction Between Hub Leakage and Mainstream Flows in Highly-Loaded High Pressure Turbine Blades," ASME. Journal of Engineering for Gas Turbines and Power, 135(6), 061014.

[6] Schneider, C.M., Schrack, D., Rose, M.G., Staudacher, S., Guendogdu, Y. and Engel, K., 2014, "On the interaction of streamwise vorticity with a rotating turbine blade," 10th Eur. Conf. Turbomach. Fluid Dyn. Thermodyn. ETC 2013, no. 1987, pp. 24–35.

[7] Schrewe, S., Werschnik, H., and Schiffer, H.P., 2013, "Experimental Analysis of the Interaction between Rim Seal and Main Annulus Flow in a Low Pressure Two Stage Axial Turbine," ASME. Journal of Turbomachinery, 135(5), 051003.

[8] Schuepbach, P., Abhari, R.S., Rose, M.G., Germain, T., Raab, I., and Gier, J., 2010, "Effects of Suction and Injection Purge-Flow on the Secondary Flow Structures of a High-Work Turbine," ASME. Journal of Turbomachinery, 132 (2), 021021.

[9]   Regina, K., Kalfas, A.I., and Abhari, R.S., 2015, "Experimental Investigation of Purge Flow Effects on a High Pressure Turbine Stage," ASME. Journal of Turbomachinery, 137 (4), 041006.

[10]   Graftieaux, L., Michard, M., and Grosjean, N., 2001, "Combining PIV, POD and vortex identification algorithms for the study of unsteady turbulent swirling flows," Measurement Science and Technology, 12(9), p. 1422.

[11]   Morgan, C., Babinsky, H., and Harvey, J., 2009, "Vortex detection methods for use with PIV and CFD data," Proc. 47th AIAA Aerospace Sciences Meeting, Orlando, Florida.

[12]   Simpson, C., Babinsky, H., Harvey, J., and Corkery, S., 2018, "Detecting vortices within unsteady flows when using single-shot PIV," Experiments in Fluids, 59(8), p. 125.

[13]   Jones, R. R., Pountney, O. J., Cleton, B. L., Wood, L. E., Deneys J. Schreiner, B., Carvalho Figueiredo, A. J., Scobie, J. A., Cleaver, D. J., Lock, G. D., and Sangan, C. M., 2019, "An Advanced Single-Stage Turbine Facility for Investigating Nonaxisymmetric Contoured Endwalls in the Presence of Purge Flow." ASME. Journal of Engineering for Gas Turbines and Power, 141(12): 121008.

[14]   Tropea, C., Yarin, A. L., and Foss, J. F., "Springer handbook of experimental fluid mechanics", Springer Science & Business Media, 2007.

[15]   Carvalho Figueiredo, A.J., Jones, R.R., Sangan, C.M. & Cleaver, D.J., 2020, "A borescope design tool for laser measurements in fluids", J. Optics and Lasers in Engineering, Volume 127 ,105874.

[16]   Carvalho Figueiredo, A. J., Jones, R., Pountney, O. J., Scobie, J. A., Lock, G. D., Sangan, C. M., and Cleaver, D. J., 2018, "Volumetric Velocimetry Measurements of Film Cooling Jets." ASME. Journal of Engineering for Gas Turbines and Power, 141(3): 031021

[17]   Stellmacher, M., and Obermayer, K., "A new particle tracking algorithm based on deterministic annealing and alternative distance measures," Experiments in Fluids, 28(6), pp. 506-518, 2000.